Bottom-up mechanical nanometrology of granular Ag nanoparticles thin films

Bottom-Up Mechanical Nanometrology of Granular Ag Nanoparticles Thin Films

Giulio Benetti,[†,‡,¶] Claudia Caddeo,[*,†,‡] Claudio Melis,[§] Gabriele Ferrini,[†,‡] Claudio Giannetti,[†,‡] Naomi Winckelmans,[‖] Sara Bals,[‖] Margriet J Van Bael,[⊥] Emanuele Cavaliere,[†,‡] Luca Gavioli,[†,‡] and Francesco Banfi[*,†,‡]

†*Interdisciplinary Laboratories for Advanced Materials Physics (I-LAMP), Università Cattolica del Sacro Cuore, Via Musei 41, 25121 Brescia, Italy*

‡*Dipartimento di Matematica e Fisica, Università Cattolica del Sacro Cuore, Via Musei 41, 25121 Brescia, Italy*

¶*KU Leuven, Laboratory of Solid State Physics and Magnetism, Department of Physics and Astronomy, Celestijnenlaan 200D, B-3001, Leuven, Belgium.*

§*Dipartimento di Fisica, Università degli Studi di Cagliari, Cittadella Universitaria, I-09042 Monserrato (Ca), Italy*

‖*EMAT University of Antwerp, Groenenborgerlaan 171, B-2020 Antwerp, Belgium*

⊥*KU Leuven, Laboratory of Solid State Physics and Magnetism, Department of Physics and Astronomy Celestijnenlaan 200D, B-3001, Leuven, Belgium.*

E-mail: caddeo@iom.cnr.it; francesco.banfi@unicatt.it

Abstract

Ultrathin metal nanoparticles coatings, synthesized by gas-phase deposition, are emerging as go-to materials in a variety of fields ranging from pathogens control, sensing to energy storage. Predicting their morphology and mechanical properties beyond a trial-and-error approach is a crucial issue limiting their exploitation in real-life applications. The morphology and mechanical properties of Ag nanoparticles ultrathin films, synthesized by supersonic cluster beam deposition, are here assessed adopting a bottom-up, multi-technique approach. A virtual film model is proposed merging high resolution scanning transmission electron microscopy, supersonic cluster beam dynamics and molecular dynamics simulations. The model is validated against mechanical nanometrology measurements and is readily extendable to metals other than Ag. The virtual film is shown to be a flexible and reliable predictive tool to access morphology-dependent properties such as mesoscale gas-dynamics and elasticity of ultrathin films synthesized by gas-phase deposition.

INTRODUCTION

Nanoparticles (NPs) ultrathin films are emerging as one of the most promising solutions in many technological applications,[1] ranging from medicine[2–5] to sensing[6–8] and energy storage.[9,10]

In this context supersonic cluster beam deposition (SCBD) is a viable technique for the production of cost-effective, high throughput metallic NPs thin films. SCBD is amenable to the deposition of a wide range of metallic NPs on virtually any substrate, while forgoing the inconveniences inherent to other synthesis methods.[11]

Despite the relevance for applications, the macroscopic mechanical parameters peculiar to SCBD-synthesized thin films remain yet to be unveiled. In situations where the NPs conserve

their individuality within the deposited film the macroscopic physical parameters are primarily ruled by the NPs connectivity pattern, i.e. by the film morphology. In these scenarios, direct assessment of the morphology poses an outstanding challenge, the films being inherently granular and their thickness in the few tens of nm range. Furthermore the availability of a cost and time effective strategy to predict NPs thin film mechanical properties beyond a trial-and-error approach is a *conditio sine qua non* to boost their deployment in any prospective application, thin films mechanical nanometrology being an open issue at the frontier of material science.[12–17]

A bottom-up approach, encompassing both experiments and computation, is here outlined to access Ag NPs thin films morphology and predict their mesoscale mechanical properties. Ag NPs have been chosen because of the availability of recent experimental data on Ag NPs films[6] against which to benchmark the results and because of their relevance in applications.[18] The approach here presented is rather general and readibly extendable to metals other than Ag.

The size-distribution of the nanoparticles and their kinetic energies are retrieved respectively from high resolution high angle annular dark field - scanning transmission electron microscopy (HAADF-STEM) and the SCBD source parameters. These specifications serve as inputs for fully atomistic molecular dynamics (MD) simulations of the NPs landing processes, ultimately resulting in a theoretically reconstructed film. The virtual film model is validated comparing its filling factor (defined as the ratio between the metal volume and the entire NPs film volume) and topography with the experimental ones. The model is then exploited to inspect the morpholoy and access the mechanical properties. As for the latter, the virtual film is first used to characterize the material porosity and the resulting gas-transport regime, relevant for mesoscale gas-dynamics applications. The virtual film is then deployed in the frame of nanoelasticity to predict the NP thin-film elastic stiffness constant. The results compares well with the value retrieved from photoacoustic nanometrology, the virtual film model thus serves as a flexible and reliable predictive tool.

METHODS

NPs film synthesis. Ag NPs are deposited at room temperature using a SCBD gas phase source. The same operative parameters are used for all the substrates (carbon grids for HAADF-STEM images and (0001) α-Al_2O_3 for all the other samples). The apparatus details and working principle have been published elsewhere[6,18,19] and are summarized in Supporting Information (SI).

High resolution HAADF- STEM. High resolution - HAADF - STEM images are collected on scattered Ag NPs deposited on an amorphous carbon grid (quantifoil) using a probe corrected FEI TITAN microscope operated at 200 kV. The following procedure, developed in the ImageJ environment,[20] is used to analyze the STEM images. A linear background is subtracted, followed by bright and dark outliers removal. Using a threshold on the gray scale intensity the bright zones are selected, isolating the z-projection of the NPs from the carbon substrate. Assuming the NPs shape to be spherical,[6,18] each single equivalent diameter is then estimated. The NPs are thus decimated by excluding the NPs matching the following criteria: NPs whose fitting ellipse aspect ratio exceeds two (usually the image of two NPs stuck together), the ones with a solidity[20] smaller than 0.6 (mainly trivial NPs due to experimental noise not eliminated by outlier removal) and the ones with a surface area inferior to 0.3 nm^2.

Molecular Dynamics. All the simulations are performed with the LAMMPS package.[21] The velocity-Verlet algorithm is used to solve the equations of motion. As for the description of the Ag-Ag interactions, a 12-6 Lennard-Jones potential[22] is used to simulate the NPs film growth whereas an Embedded Atom model Potential (EAM)[23] is adopted to estimate the film elastic constant. Further computational details are reported in the Supporting Information.

Real and reconstructed AFM. Exper-

imental AFM images are acquired using a Solver-pro NTMDT microscope, operated in semicontact mode using an Etalon HA-NC tip with a nominal radius of 10 nm. Reconstructed AFM images, computed from the virtual film obtained from the experimentally-driven MD simulation, are obtained importing raw xyz data into MATLAB and implementing the procedure detailed in SI.

Methodological note. Different NPs films were deposited and analyzed so as to verify that the data are not sample specific. Equivalently, the theoretical results were tested on various MD realizations and found to be realization-independent.

RESULTS AND DISCUSSION

Bottom-Up NPs film reconstruction

NPs size distribution in the supersonic beam. Knowledge of the size distribution of the NPs in the supersonic beam is a fundamental asset for a trustworthy film morphology reconstruction based on MD simulations. To estimate the NPs size distribution, scattered Ag NPs were directly deposited on a carbon grid and inspected via high resolution HAADF-STEM. One hundred images, similar to the one presented in Figure 1a, were analyzed as previously explained in the methods section.

The resulting distribution, histogrammed in log scale in Figure 1b, is bimodal and is conveniently split in two sets. Set S (green color in Figure 1b) groups "small" NPs - diameters up to 4.1 nm - and has cardinality N_S, accounting for 84% of the total NPs number and 5.4% of the total deposited mass. Set B (blue color in Figure 1b) groups "big" nanoparticles - diameters exceeding 4.1 nm - and has cardinality N_B, accounting for the remaining 16% of the total NPs number and 94.6% of the total deposited mass.

In strict terms TEM images allow access to the projected shape of the NPs deposited on the amorphous carbon TEM grid. The question then arises as whether the NPs size distribution obtained from TEM is indicative of the actual size distribution of NPs in the supersonic beam. While deformation of NPs could potentially occur due to collision and interaction with the grid substrate, it was observed that, when the kinetic energy per atom, K, is significantly lower than the cohesion energy of the atoms in the NP, C, the 3D shape of the NPs in flight is retained after landing on the soft grid substrate.[24–27] This was observed for instance for clusters produced by an inert gas laser-driven vaporization source, for which Ref. 25 reported an average K=0.33 eV/atom versus C=5.84 eV/atom yielding $K/C = 0.05$-0.06. In the present case, for Ag NPs with K=0.2 eV/atom (this value will be addressed shortly) and C=2.98 eV/atom,[28] K/C reads 0.068. The NPs are thus expected to retain their 3D shape once landed on the grid substrate.

For the sake of computational convenience a coarse-grained version of the experimental size distribution was adopted. The NPs within each set S and B are replaced with monodispersed NPs of volumes (diameters) V_S (d_S) and V_B (d_B) respectively, while conserving the cardinality of each original set. The volumes are chosen so as to grant the same deposited volume as in the original distribution: $N_S V_S = \sum_{\{S\}} V_i$ and $N_B V_B = \sum_{\{B\}} V_i$, the sum being performed on the NPs in sets S and B respectively. The resulting values are V_S=2.15 nm^3 and V_B=195.4 nm^3, yielding equivalent diameters d_S=1.6 nm and d_B= 7.2 nm, where $d_{S,B}$ are taken such that $(4\pi/3)(d_{S,B}/2)^3$=V$_{S,B}$. This coarse-graining approach ensures the same deposited mass in simulations and real experiments, while preserving the total NPs number [1] and N_B/N_S ratio.

Energy of the landing NPs. NPs deformation can occur due to collisions between NPs deposited in subsequent shots (the plasma source is pulsed, refer to SI for further details on the plasma source). The film morphology thus critically depends on the average kinetic energy per atom of the landing clusters.

[1] The present choice is at variance with respect to the simple average value of the diameters, yielding 1.3 and 6.8 nm for set S and B respectively

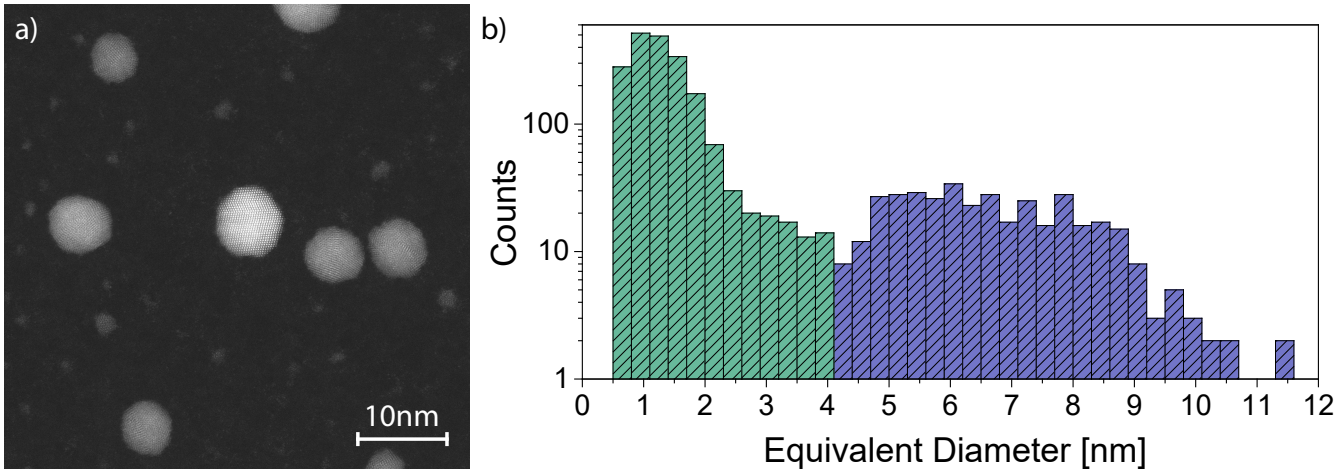

Figure 1: a) High Resolution HAADF-STEM image of scattered metallic Ag NPs. b) Size distribution in log scale obtained analysing 100 STEM images of the as deposited NPs. The two colored regions indicate the partition into small (green) and big (blue) NPs, see main text for further details.

To estimate the average K as a function of the cluster dimension, two parameters, specific for the SCBD source, need to be retrieved: the carrier gas asymptotic velocity v_{He} and the ablation source parameter δ. In fact, the size-dependent cluster velocity, obtained in the frame of the Wrenger-Meiwes Broer model[29] under a purely elastic NP-gas collision regime, reads:

$$v(N) = v_{He}\left[1 - \left(\frac{N - m_{He}/m_{at,NP}}{N + m_{He}/m_{at,NP}}\right)^{N^{2/3}\delta}\right] \quad (1)$$

where N is the number of atoms forming a cluster, $m_{at,NP}$ and m_{He} the atomic masses of the atomic species composing the clusters and the carrier gas (Helium) respectively. In order to estimate the parameters v_{He} and δ, a fit based on Eq.1 was performed on mass spectrometry - time of flight data acquired by Mazza *et al.*[30] on Ti clusters. The data were collected exploiting a SCBD source with the same geometrical features as the one used in the present work (see SI).

Given an effective residence time $\sim$ 20 ms (this value is an average of all the NPs residence times within a shot, the residence time being defined as the time spent by a NP in the ablation chamber before expulsion from it through the supersonic beam),[30] the values v_{He} and δ were here retrieved. With these two values at hand, and making use of Eq. 1 contextualized in the present case, that is with $m_{at,NP}$=m_{Ag} (in the present work Ag clusters are addressed as opposed to Ti; He is used as the carrier gas), one obtains K_B=0.20 eV/atom for NPs in set B and K_S=0.59 eV/atom for NPs in set S.

Virtual NP film. A reliable NPs film model can now be reconstructed implementing MD simulations based on experimental inputs. The virtual NPs film was obtained by simulating multiple landing of 500 Ag NPs, deposited in 5 steps. The NPs where first assembled with a full atomistic approach. According to the experimental data, the clusters vibrational temperatures before the impact is 300 K. Therefore, the NPs were equilibrated with a thermostat at 300 K for 150 ps. The thermostat was then switched off prior to simulating the deposition process. The NPs population was constructed with 16% of the clusters of diameters d_B=7.2 nm (set B) and 84% of diameters d_S=1.6 nm (set S), thus complying with the coarse-grained experimental NPs size-distribution. As for the deposition process, the first 100 NPs were placed at random positions on top of the substrate to simulate a multiple impact. Initial velocities, calculated from the K_B and K_S values, were assigned to the NPs. The average kinetic energies per atom of the landing clusters were fixed to K_B=0.20 eV/atom (set B) and K_S=0.59

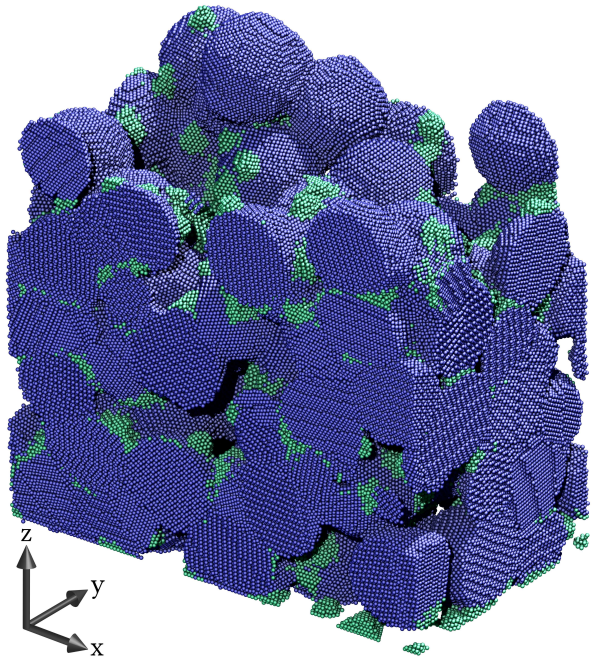

Figure 2: Rendering of the virtual NPs thin film obtained as the final state of the experiments-driven MD simulations. The Ag atoms composing big (set B) and small (set S) NPs are colored in blue and green respectively, maintaining the same color code as in Figure 1b. The average film thickness is $\langle \tilde{z} \rangle = 29$ nm.

eV/atom (set S), consistently with the results obtained from the analysis of the SCBD process. Periodic boundary conditions were applied in the x-y direction. Finally, the NPs were left free to evolve according to pure Newtonian dynamics.[31] Further computational details are reported in SI.

The nanoporous film model is represented in Fig.2. The cell has a base size $L_x \times L_y$=35×20 nm^2 and lays in the z=0 plane. Reticulating the cell's base with domains of sizes $dxdy$=0.5×0.5 nm^2, the average film thickness reads $\langle \tilde{z} \rangle = 29$ nm, where $\tilde{z}(x,y)$ is the top-most atom z-coordinate in the $dxdy$ domain centered around the point of coordinates (x,y) (refer to SI for details). The film is indeed granular, the core of the scaffold structure being dictated by "big" NPs (blue atoms in Figure 2) that, despite some degree of deformation, substantially preserve their individuality. The "small" NPs are, on the contrary, more deformed. This is consistent with the experimental K/C values, K_S/C_S being 0.2 as opposed to K_B/C_B=0.068. The film morphology is better appreciated inspecting the simulation cell from different directions (see Multimedia file in SI).

Benchmarking the virtual film model. In order to reliably predict morphology-dependent quantities, the virtual film morphology has first to be benchmarked against significant experimental figures, namely the film filling factor and topography, as obtained on a SCBD-deposited Ag NPs films fabricated for the purpose [2]. The filling factor, calculated from the virtual film, reads 0.73 ± 0.05, in good agreement with the experimental value[6] of 0.80±0.06 obtained from X-ray measurements. The *experimental* AFM topography $h(x,y)$=$t_F(x,y)$-$\langle t_F \rangle$, measured in tapping mode on a 30 nm thick film, is reported in Figure 3a (235×235 nm^2 scan area, tip radius 10 nm, pixel size 0.5 nm^2). The function $t_F(x,y)$ is the film thickness, referenced to the supporting substrate, as measured with an AFM tip positioned in the point of coordinates (x,y) whereas $\langle t_F \rangle$ is its spatial average. The information content is synthesized in Figure 3c where the normalized occurences of $h(x,y)$ are histogrammed in full gray. The *theoretical* AFM topography was reconstructed starting from the virtual solid and accounting for tip finite-size effects. This was achieved by computing $h(x,y)$ starting from $\tilde{z}(x,y)$ and from the AFM tip parameters (refer to SI for details on the computation). For the sake of comparison with the experimental height distribution, the reconstructed distribution statistics was increased by analysing intermediate states of MD simulations - under the assumption that the coating's Root Mean Square (RMS) roughness is not influenced by its thickness. This ansatz is supported by the analysis of the surface texture of each intermediate state in terms of image uniformity and entropy (refer to SI). The virtual AFM images, reported in Figure 3b, were obtained from subsequent MD steps, *i.e.* reconstructing films with average thicknesses $\langle t_F \rangle$ of 9, 14, 23, 27 and 31 nm accounting for AFM-tip

[2]The experiments were performed on films obtained exploiting the same SCBD parameters as the one exploited to deposit the NPs for the size-distribution investigation.

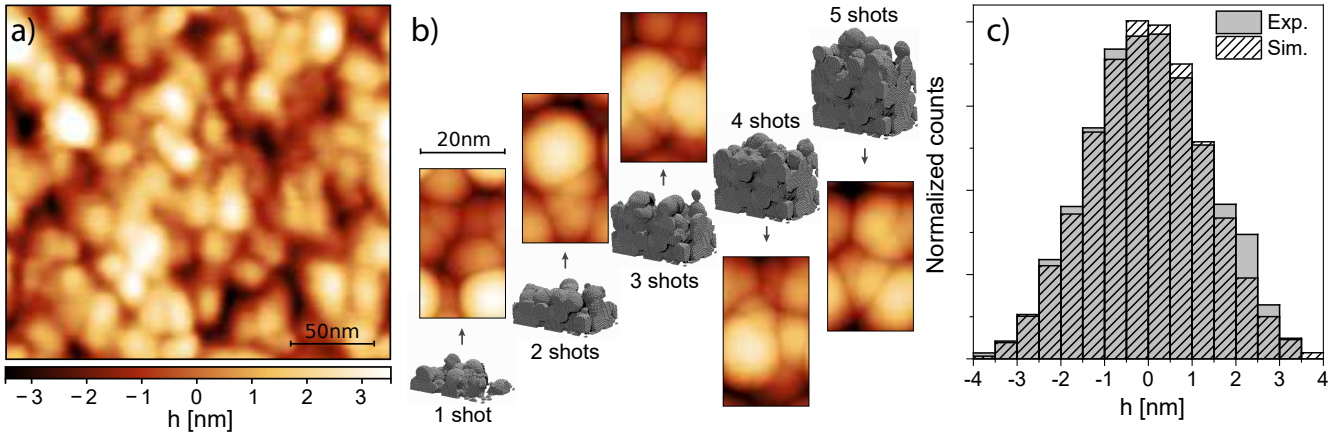

Figure 3: a) Experimental AFM image obtained from a SCBD-deposited Ag NPs thin film of average thickness 30 nm. b) Theoretical AFM images obtained from virtual films. These images are obtained starting from intermediate steps of the MD simulations, *i.e.* subsequent shots of the simulation resulting in films of average thickness $\langle t_F \rangle$ = 9, 14, 23, 27 and 31 nm for shots one through five. The calculated thickness $\langle t_F \rangle$ accounts for AFM-tip convolution effects. c) Comparison between the normalised height distribution - referenced to the film average height - of the experimental (gray) and reconstructed (patterned) AFM images.

convolution effect (corresponding to the average non-convoluted thicknesses $\langle \tilde{z} \rangle$ = 5.0, 10.8, 16.4, 22.8 and 28.6 nm). The patterned histogram (slant black line on white background) reports the normalized occurrences of $h(x, y)$ obtained from the five height distributions relative to the reconstructed solids of Figure 3b. The overlap between the virtual and experimental films topography is excellent, both upon visual inspection of the two histograms and comparing their standard deviations: 1.37 nm (simulated) vs 1.33 nm (experimental). These evidences confirm the reliability of the model film morphology.

A debated issue, when discussing granular thin-films morphologies, is whether the film is affected by z-dependent densification phenomena, or, otherwise stated, whether the slicing filling factor varies with the z coordinate[3]. This piece of information escapes direct experimental evidence but may be obtained from the virtual film model.

Figure 4 reports the slice filling factor vs the z coordinate calculated for films obtained from the five intermediate MD simulation steps. The corresponding virtual films are visualized in inset of Figure 4 for ease of reading.

Let's focus for instance on the graph corresponding to the film obtained with five shots (blu curve in Figure 4), the behaviour for other film thicknesses being alike. The slicing filling factor reaches a plateau value within the first 5 nm, a small modulation (10% peak-to-peak maximum relative variation) being superposed on the otherwise constant background (the reason for the somewhat different plateau build-up inherent the thinner film is discussed further on). Thickness related densification phenomena are therefore ruled out. This fact may be further appreciated noting the similarities among xy cross-sectional views of the void structure taken at different z coordinates of the virtual film, see Figure 5. Referring back to Figure 4, for values of z approaching the film's upper surface the slicing filling factor monotonously drops to zero, this being a genuine surface effect[4]. This fact precludes a clear build up of

[3]The slicing filling factor is here defined as the filing factor computed in a rectangular cuboid of size $L_x \times L_y \times \Delta z$=35×20×0.5 nm^3 centered at a coordinate z

[4]This drop is due to z reaching the surface region. In this context, the surface region is characterized by z coordinate values for which the film surface falls within the rectangular cuboid of size $L_x \times L_y \times \Delta z$ nm^3 exploited to calculate the slicing filling factor.

the plateau region for the thinner film of average height $\langle\tilde{z}\rangle$ =5 nm.

Furthermore, the impacting NPs from subsequent shots do not modify the underlying NPs and film morphology. This fact may be recognized observing the overlap among the slice filling factors calculated for films of different average thicknesses, that is obtained with increasing NPs shots, for z coordinates out of the surface region.

Interestingly enough, the present results bear some similarities with those obtained modelling aerosol-based NPs depositions processes in the ballistic regime[32] by solving the Langevin equation of motion.[33] The dynamics of nanoparticles in the gas-phase, as the one addressed in Ref. 32, encompasses both a deterministic particle motion and a nondeterministic particle random walk. The relative importance of these two effects is conveniently assessed by means of the Peclet number, Pe.[34] For $Pe \gg 1$ the deterministic particle motion is dominant, setting the dynamics in the ballistic regime. In the opposite limit of $Pe \ll 1$ the nondeterministic particle random walk dominates, leading to a diffusive dynamics. Despite the different deposition technique and an exiguous statistics (as compared to the NPs number addressed in Ref. 32), the latter dictated by the MD approach, the sliced filling factor calculated for the present case (see Figure 4) has a shape comparable with that reported in Ref. 32 for the ballistic case, i.e. Pe=100. Specifically, a constant slicing filling factor plateau is here reached (even though with a different plateau value as compared to Ref. 32) with tiny oscillations superposed on the otherwise constant background. The latter occurrence does not seem fortuitous: normalizing the z coordinate against the big NPs diameter d_B=7.2 nm, the first oscillation maximum is here obtained for a normalized z-quota of 0.75, the second maximum for ∼1.4, these values being consistent with the explanation given in Ref. 32. These observations set the present findings in a more general frame.

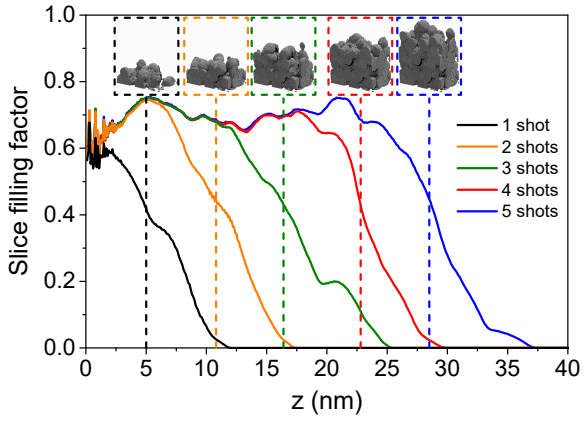

Figure 4: Slice filling factor vs z coordinate. The colors identify results from the intermediate simulation steps shown in inset. The vertical dashed lines indicate the average thickness $\langle\tilde{z}\rangle$ = 5.0, 10.8, 16.4, 22.8 and 28.6 nm of the virtual films. The calculated height $\langle\tilde{z}\rangle$ does not account for AFM-tip convolution effects.

Mechanical nanometrology and applications.

The NPs film model may be employed to access a variety of morphology-related properties, among which gas-dynamics and elastic properties.

Mesoscale gas-dynamics. The NPs film is inherently porous, see Fig.2. This fact, together with the possibility of spraying the NPs on virtually any surface, makes the film potentially appealing for distributed gas-dynamics applications. To this aim knowledge of the pores connectivity pattern - open vs closed porosity - and the transport mechanism ruling the gas dynamics is required. The gas transport regime - viscous vs molecular - is discriminated on the basis of the Knudsen number $K_n = \lambda/L$. The molecular mean free path λ is the average distance traveled by a molecule between two scattering events with other molecules, L is the physical length ruling the scattering event between the gas molecule and the NPs film scaffold. The estimate of L for the present case will be discussed shortly. In the viscous transport regime the molecule-molecule scattering events prevail over the molecule-pore wall scattering ones, resulting in K_n <1. In the molecular transport regime the opposite is true, resulting in K_n >1.

To which extent K_n should deviate from unity in order for transport to be defined as viscous or molecular depends on the application field. In the frame of vacuum technology,[35] for instance, the regime is considered viscous (molecular) for K_n <0.01 (K_n >5).

Figure 5 reports the void structure, i.e. the complementary of the NPs scaffold shown in Figure 2. The pores are connected (see Multimedia file in SI to better appreciate this fact), thus allowing for gas/fluid transport across the film. The film porosity, as calculated from the virtual film model, is ϕ=V_p/V=0.27±0.05, V_p being the voids volume and V the total NPs film volume.

In order to estimate the pore size relevant to gas-transport, i.e. obtain an estimate for L, xy plane cross-sections where taken at several z-quotas of the void scaffold, the spacing between cross sections being 0.25 nm. Samples images are reported in Figure 5 (a)-(e). Given the random nature of the voids cross-sectional geometry, estimating L implies some degree of arbitrariness. Although the pores cross-section geometry varies extensively, see Figure 5, some general guiding principles may be obtained by considering the ideal case of a cylindrical void of cross sectional radius r. The conductivity of a pipe of radius r scales as r^4 for viscous laminar flow and as r^3 in the molecular regime. These scaling laws suggest considering, within each section, the pore of wider surface area to be the one playing by far the main role in gas transport. Hence, for the purpose of estimating L, the average pore section area $\bar{A}_p$= 80 nm^2 has been estimated as the arithmetic mean of the areas of the most extended pore sections of each z-plane. Substituting, for the sake of gas transport, the actual pores with "effective" pores of circular section, the resulting physical length ruling the scattering between the Ag scaffold and the gas molecules reads L=$\sqrt{\bar{A}_p/\pi}$ ≈ 5 nm. Since the actual voids cross-sections are not circular, this value constitutes an overestimation of the effective L. This fact may be further appreciated upon visual inspection of the cross-sectional cuts shown in Figure 5 (a)-(e). The pores cross-sections elongate along certain directions and constrict along the orthogonal

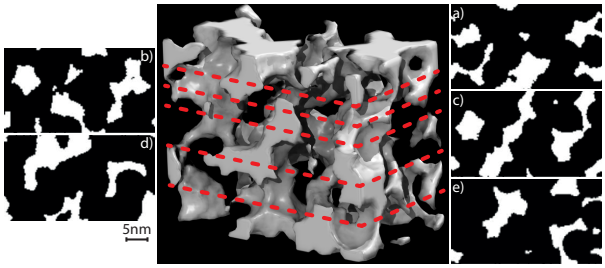

Figure 5: Void structure. The white 3D scaffold represents the voids between the deposited NPs. The image has been cut at a quota z=25 nm for ease of visualisation. Stacking of the xy cross-sectional views may be thought of as composing the z-axial tomography of the void scaffold. Panels (a)-(e): cross-sectional cuts taken across planes of the void scaffold at different z-coordinates, as indicated by the red-dashed lines. The 5 nm scale bar refers to the cross-sectional cuts.

ones, the narrow size measuring, in most realisations, less than the 5 nm bar-length. For the sake of evaluating L the narrower extension is the relevant one, which is overestimated by assuming an "effective" circular pore cross-section.

Within the hard-sphere approximation, the molecular mean free path reads:

$$\lambda = \frac{k_B T}{\sqrt{2}\pi d_0 P} \qquad (2)$$

k_B being the Boltzman constant, T and P the gas temperature and pressure respectively, and d_0 the molecular diameter. Assuming P=101 KPa and T=288 K (Standard International Atmosphere, SIA) and indicative values of d_0 in the range[36] 0.26 nm (Helium) to 0.44 nm (Clorine), one finds $\lambda \sim$ 50 - 150 nm. An upper-bound estimation of L=5 nm, as retrieved from the previous analysis on porosity, results in K_n ∼10 - 30, thus setting gas transport across the NP film in the molecular (Knudsen) regime.

The open-porosity and the Knudsen regime here predicted for gas transport, together with the possibility of depositing the film on any surface with high deposition throughputs, makes the NPs film an appealing inorganic mesoporous membrane for distributed membrane-

based gas separation.[37,38] Following reference 39, the figure of merit for gas separation in membranes is selectivity, $\alpha_{A/B}=\bar{P}_A/\bar{P}_B$, where $\bar{P}_A$ and $\bar{P}_B$ are the permeabilities of the gas species A and B. A value $\alpha_{A/B}=1$ means the membrane is not effective in separating the gas species, whereas any other value will imply some degree of separation among the two gasses. For low enough pressures, so as for Henry's law to be valid, $\bar{P}_i=D_iS_i$ with D_i and S_i the diffusion and solubility coefficients of gas species i (i=A, B), resulting in $\alpha_{A/B}=(D_A/D_B)(S_A/S_B)$. In situations where the gas species to be separated are chemically similar, i.e $(S_A/S_B)\sim1$, the selectivity process is diffusion-driven. In the molecular transport regime[40] $D_i=(d_{0,i}/3)\sqrt{8RT/\pi m_i}$, where m_i and $d_{0,i}$ are the molar mass and molecular diameter of gas species i and R is the ideal gas constant. The NPs film could thus serve as a membrane separating the gas species on the basis of their molecular masses and molecular diameters, selectivity reading $\alpha_{A/B}=(d_{0,A}/d_{0,B})\sqrt{m_B/m_A}$. For instance, in the industrially relevant case of the ammonia synthesis process the purge gas is composed of an H_2/N_2 mixture.[41] The recovery of the two gas species is an important aspect, reducing both energy and environmental costs. Given values of m_{H_2}=2.02 g/mol, m_{N_2}=28.01 g/mol, d_{0,H_2}=2.89 Å and d_{0,N_2}=3.64 Å[42] the membrane selectivity reads $\alpha_{H_2/N_2}\sim3$, thus allowing the two species to be effectively separated.

Nanoelasticity. Assessment of the elastic properties of ultra-thin coatings is a remarkable problem in materials science and the prerequisite to any perspective application. The reconstructed film is now exploited to predict the stiffness constant along the film growth direction, the mechanical properties being essentially ruled, in the present case, by the film morphology. This quantity is relevant in a variety of applications. For instance it rules the operating frequency range of NPs thin film-based hypersonic photo-acoustic transducers.[6] The elastic constant C_{11} of the NPs film has been calculated on the previously obtained scaffold by using an Embedded Atom model Potential (EAM).[23] The EAM is built with functions that have been empirically determined in order to specifically match the elastic constants of pure Face-centered cubic (fcc) metals. For this reason such a model potential is more suitable with respect to the previously used Lennard-Jones pair-potential to describe the elastic properties of the NPs film. However, the high computational cost of the EAM potential prevents its use to perform a NPs deposition simulation of a system containing a number of atoms as large as 1.1×10^6, necessary to obtain a NP film model of realistic size (see Figure 2).

In order to estimate C_{11} an uniaxial (along the deposition direction) deformation is applied to the virtual film with an overall strain varying in the range ±5%. At each deformation step the sample is fully relaxed by means of a conjugate gradient optimisation. By fitting the energy-strain curve with a parabolic function a value C_{11}=89 ± 6 GPa is obtained at a temperature of T=0 K. The elastic constants are monotonously decreasing with temperature. For the sake of comparison the room temperature experimental value $C_{11,Exp}$(300 K)=70±5 GPa, obtained on equivalent NPs films investigated by means of time-resolved optoacoustics experiments,[6] reads, once rescaled to T=0 K, $C_{11,Exp}$(0 K)=75±5 GPa (refer to SI for details). The theoretical and experimental values are in pretty close agreement. As a further consistency check, the ratio between the C_{11} measured on the NPs film and on single crystal bulk Ag[43] at room temperature reads 0.57 ± 0.04. The same ratio obtained from MD simulations at 0 K - using the same potential for the NP film and the Ag bulk - is 0.62 ± 0.07. The compatibility of these values confirms the validity of the adopted approach.

The present strategy is readily generalisable to SCBD-deposited NPs thin film other than pure Ag. Fcc elemental metals and their alloys are successfully described by means of suitable model potentials, thus potentially providing the correct morphology as well as mechanical properties for technologically relevant films.

The bottom-up approach to the SCBD-deposited metal NPs film morphology has far reaching applications in fields other than mesoscale gas-dynamics and nanoelasticity.

The experimentally-driven model will allow engineering, beyond a trial and error approach, the granular films optical[44,45] properties, the interaction of the mesoporous scaffolds with liquids,[46] pathogens,[2] proteins[47] and biofilms[48,49] and their exploitation in nanojoining technology[50] and wearable electronics.[51]

CONCLUSIONS

In conclusion, the morphology and mechanical properties of Ag nanoparticles ultrathin films, synthesized by supersonic cluster beam deposition, have been investigated adopting a multi-technique bottom-up approach. Combining high resolution - high angle annular dark field scanning transmission electron microscopy, analysis of the gas-dynamics inherent supersonic cluster beam deposition with molecular dynamics simulations, a granular NPs virtual film was reconstructed. The model has been validated comparing the computed topography and filling factor against the experimental values from AFM and X-ray measurements. The virtual sample allowed to investigate the film porosity and gas-dynamics through the NPs film. In this context the Knudsen regime was recognised as the leading transport mechanism. This fact opens the possibility of exploiting the NPs films as mesoscopic membranes for gas separation. The virtual sample was then exploited to access the C_{11} elastic constant, mechanical nanometrology of ultra-thin granular films being an outstanding open issue in material science. The results are compatible with experimental values obtained from ultra-fast optoacoustic nanometrology. The approach here presented is extendable to other metallic granular films and bears great interests for material science applications ranging from nanosensing, nanooptomechanics to nanomedicine.

SUPPORTING INFORMATION

Supporting Informations are provided on the following topics: SCBD source geometry, MD simulation details, Filling factor and AFM topography from the virtual Nanoparticle film, AFM images comparison: surface texture analyses, Rescaling of the $C_{11;exp}$ value to low temperature. Two videos (Multimedia files) are provided illustrating the NPs film morphology and void structure.

AUTHOR INFORMATIONS

Corresponding Authors
Phone: +39 030 2406 709. Fax: +39 030 2406 742. E-mail: francesco.banfi@unicatt.it (F.B.). Phone: +39 070 6754875. Fax: +39 070 6754892. E-mail: caddeo@iom.cnr.it (C.C.).

Notes
The authors declare no competing financial interest.

ACKNOWLEDGEMENTS

All the authors thank Prof. Dr. Luciano Colombo for enlightening discussions. C.C and F.B acknowledge financial support from the MIUR Futuro in ricerca 2013 Grant in the frame of the ULTRANANO Project (project number: RBFR13NEA4). F.B, G.F and C.G acknowledge support from Università Cattolica del Sacro Cuore through D.2.2 and D.3.1 grants. F.B acknowledge financial support from Fondazione E.U.L.O. The authors acknowledge financial support from the European Union through the 7th Framework Program (FP7) under a contract for an Integrated Infrastructure Initiative (Reference No. 312483 ESTEEM2).

References

(1) Stark, W. J.; Stoessel, P. R.; Wohlleben, W.; Hafner, A. Industrial Applications of Nanoparticles. *Chem. Soc. Rev.* **2015**, *44*, 5793–5805.

(2) Benetti, G.; Cavaliere, E.; Canteri, A.; Landini, G.; Rossolini, G. M.; Pallec-

chi, L.; Chiodi, M.; Van Bael, M.; Winckelmans, N.; Bals, S. et al. Direct Synthesis of Antimicrobial Coatings Based on Tailored Bi-Elemental Nanoparticles. *APL Mat.* **2017**, *5*, 036105.

(3) Rameshkumar, P.; Saranya, S.; Sujatha, K.; Ramaraj, R. In Situ Formation of Gold/silver Bi-Metal Nanodots on Silica Spheres and Evaluation of Their Microbicidal Properties. *RSC Adv.* **2015**, *5*, 5038–5045.

(4) Boisselier, E.; Astruc, D. Gold Nanoparticles in Nanomedicine: Preparations, Imaging, Diagnostics, Therapies and Toxicity. *Chem. Soc. Rev.* **2009**, *38*, 1759–1782.

(5) Kholmanov, I. N.; Stoller, M. D.; Edgeworth, J.; Lee, W. H.; Li, H.; Lee, J.; Barnhart, C.; Potts, J. R.; Piner, R.; Akinwande, D. et al. Nanostructured Hybrid Transparent Conductive Films With Antibacterial Properties. *ACS Nano* **2012**, *6*, 5157–5163.

(6) Peli, S.; Cavaliere, E.; Benetti, G.; Gandolfi, M.; Chiodi, M.; Cancellieri, C.; Giannetti, C.; Ferrini, G.; Gavioli, L.; Banfi, F. Mechanical Properties of Ag Nanoparticle Thin Films Synthesized by Supersonic Cluster Beam Deposition. *J. Phys. Chem. C* **2016**, *120*, 4673–4681.

(7) Wegner, K.; Vinati, S.; Piseri, P.; Antonini, a.; Zelioli, a.; Barborini, E.; Ducati, C.; Milani, P. High-Rate Production of Functional Nanostructured Films and Devices by Coupling Flame Spray Pyrolysis With Supersonic Expansion. *Nanotechnology* **2012**, *23*, 185603.

(8) Nasiri, N.; Bo, R.; Hung, T. F.; Roy, V. A.; Fu, L.; Tricoli, A. Tunable Band-Selective UV-Photodetectors by 3D Self-Assembly of Heterogeneous Nanoparticle Networks. *Adv. Funct. Mater.* **2016**, *26*, 7359–7366.

(9) Kubacka, A.; Fernández-García, M.; Colón, G. Advanced Nanoarchitectures for Solar Photocatalytic Applications. *Chem. Rev.* **2011**, *112*, 1555–1614.

(10) Liu, C.-J.; Burghaus, U.; Besenbacher, F.; Wang, Z. L. Preparation and Characterization of Nanomaterials for Sustainable Energy Production. *ACS Nano* **2010**, *4*, 5517–5526, PMID: 20973572.

(11) Wegner, K.; Piseri, P.; Tafreshi, H. V.; Milani, P. Cluster Beam Deposition: A Tool for Nanoscale Science and Technology. *J. Phys. D: Appl. Phys.* **2006**, *39*, R439.

(12) Hoogeboom-Pot, K. M.; Turgut, E.; Hernandez-Charpak, J. N.; Shaw, J. M.; Kapteyn, H. C.; Murnane, M. M.; Nardi, D. Nondestructive Measurement of the Evolution of Layer-Specific Mechanical Properties in Sub-10 Nm Bilayer Films. *Nano Lett.* **2016**, *16*, 4773–4778.

(13) Hass, G.; Francombe, M. H.; Hoffman, R. W. *Physics of Thin Films: Advances in Research and Development*; Elsevier, 2013.

(14) Nardi, D.; Travagliati, M.; Murnane, M. M.; Kapteyn, H. C.; Ferrini, G.; Giannetti, C.; Banfi, F. Impulsively Excited Surface Phononic Crystals: A Route Toward Novel Sensing Schemes. *IEEE Sens. J.* **2015**, *15*, 5142–5150.

(15) Travagliati, M.; Nardi, D.; Giannetti, C.; Gusev, V.; Pingue, P.; Piazza, V.; Ferrini, G.; Banfi, F. Interface Nano-Confined Acoustic Waves in Polymeric Surface Phononic Crystals. *Appl. Phys. Lett.* **2015**, *106*, 021906.

(16) Peli, S.; Nembrini, N.; Damin, F.; Chiari, M.; Giannetti, C.; Banfi, F.; Ferrini, G. Discrimination of Molecular Thin Films by Surface-Sensitive Time-Resolved Optical Spectroscopy. *Appl. Phys. Lett.* **2015**, *107*, 163107.

(17) Hettich, M.; Jacob, K.; Ristow, O.; Schubert, M.; Bruchhausen, A.; Gusev, V.; Dekorsy, T. Viscoelastic Properties and Efficient Acoustic Damping in Confined

Polymer Nano-Layers at GHz Frequencies. *Scientific reports* **2016**, *6*, 33471.

(18) Cavaliere, E.; De Cesari, S.; Landini, G.; Riccobono, E.; Pallecchi, L.; Rossolini, G. M.; Gavioli, L. Highly Bactericidal Ag Nanoparticle Films Obtained by Cluster Beam Deposition. *Nanomedicine: NBM* **2015**, *11*, 1417–1423.

(19) Chiodi, M.; Cheney, C. P.; Vilmercati, P.; Cavaliere, E.; Mannella, N.; Weitering, H. H.; Gavioli, L. Enhanced Dopant Solubility and Visible-Light Absorption in Cr-N Codoped TiO_2 Nanoclusters. *J. Phys. Chem. C* **2012**, *116*, 311–318.

(20) Ferreira, T.; Rasband, W. ImageJ User Guide. *IJ1. 46r. Natl. Inst. Health, Bethesda, MD.* **2012**,

(21) Plimpton, S. Fast Parallel Algorithms for Short-Range Molecular Dynamics. *J. Comput. Phys.* **1995**, *117*, 1–19.

(22) Heinz, H.; Vaia, R. A.; Farmer, B. L.; Naik, R. R. Accurate Simulation of Surfaces and Interfaces of Face-Centered Cubic Metals Using 12-6 and 9-6 Lennard-Jones Potentials. *J. Phys. Chem. C* **2008**, *112*, 17281–17290.

(23) Foiles, S. M.; Baskes, M. I.; Daw, M. S. Embedded-Atom-Method Functions for the Fcc Metals Cu, Ag, Au, Ni, Pd, Pt, and Their Alloys. *Phys. Rev. B* **1986**, *33*, 7983–7991.

(24) Alayan, R.; Arnaud, L.; Broyer, M.; Cottancin, E.; Lermé, J.; Vialle, J. L.; Pellarin, M. Morphology and Growth of Metal Clusters in the Gas Phase: A Transition From Spherical to Ramified Structures. *Phys. Rev. B* **2006**, *73*, 125444.

(25) Alayan, R.; Arnaud, L.; Bourgey, a.; Broyer, M.; Cottancin, E.; Huntzinger, J.; Lermé, J.; Vialle, J.; Pellarin, M.; Guiraud, G. Application of a Static Quadrupole Deviator to the Deposition of Size-Selected Cluster Ions From a Laser Vaporization Source. *Rev. Sci. Instrum.* **2004**, *75*, 2461–2470.

(26) Schouteden, K.; Lauwaet, K.; Janssens, E.; Barcaro, G.; Fortunelli, A.; Van Haesendonck, C.; Lievens, P. Probing the Atomic Structure of Metallic Nanoclusters With the Tip of a Scanning Tunneling Microscope. *Nanoscale* **2014**, *6*, 2170–2176.

(27) Schouteden, K.; Lando, A.; Janssens, E.; Haesendonck, C. V.; Lievens, P. Morphology and Electron Confinement Properties of Co Clusters Deposited on Au(111). *New J. Phys.* **2008**, *10*, 083005.

(28) Kittel, C. *Introduction to Solid State Physics*; Wiley, 1971.

(29) Wrenger, B.; Meiwes-Broer, K. The Application of a Wien Filter to Mass Analysis of Heavy Clusters From a Pulsed Supersonic Nozzle Source. *Rev. Sci. Instrum.* **1997**, *68*, 2027–2030.

(30) Mazza, T.; Devetta, M.; Milani, P.; Bongiorno, G.; Coreno, M.; Piseri, P. Accessing the Fractal Dimension of Free Clusters in Supersonic Beams. *New J. Phys.* **2011**, *13*, 023009.

(31) Cardia, R.; Melis, C.; Colombo, L. Neutral-Cluster Implantation in Polymers by Computer Experiments. *J. Appl. Phys.* **2013**, *113*, 224307.

(32) Nasiri, N.; Elmøe, T. D.; Liu, Y.; Qin, Q. H.; Tricoli, A. Self-Assembly Dynamics and Accumulation Mechanisms of Ultra-Fine Nanoparticles. *Nanoscale* **2015**, *7*, 9859–9867.

(33) Elmøe, T. D.; Tricoli, A.; Grunwaldt, J.-D.; Pratsinis, S. E. Filtration of Nanoparticles: Evolution of Cake Structure and Pressure-Drop. *J. Aerosol Sci.* **2009**, *40*, 965–981.

(34) Rodríguez-Pérez, D.; Castillo, J. L.; Antoranz, J. C. Relationship Between Particle Deposit Characteristics and the Mech-

anism of Particle Arrival. *Phys Rev E* **2005**, *72*, 021403.

(35) Hoffman, D.; Singh, B.; Thomas III, J. H. *Handbook of Vacuum Science and Technology*; Academic Press, 1997.

(36) Hirschfelder, J. .; Curtiss, C.; Bird, R. *Molecular Theory of Gases and Liquids*; American Association for the Advancement of Science, 1954; Vol. 120; pp 516–517.

(37) Koros, W.; Fleming, G. Membrane-Based Gas Separation. *J. Membr. Sci.* **1993**, *83*, 1–80.

(38) Baker, R. W.; Low, B. T. Gas Separation Membrane Materials: A Perspective. *Macromolecules* **2014**, *47*, 6999–7013.

(39) Javaid, A. Membranes for Solubility-Based Gas Separation Applications. *Chem. Eng. J.* **2005**, *112*, 219–226.

(40) Gilron, J.; Soffer, A. Knudsen Diffusion in Microporous Carbon Membranes With Molecular Sieving Character. *J. Membr. Sci.* **2002**, *209*, 339–352.

(41) Kajama, M. N.; Nwogu, N. C.; Gobina, E. Preparation and Characterization of Inorganic Membranes for Hydrogen Separation. *Int. J. Hydrogen Energy* **2016**, *41*, 8221–8227.

(42) Marr, R.; Draxler, J.; Ho, W.; Sirkar, K. In *Membrane Handbook*; Ho, W. S. W., Ed.; Springer US: Boston, MA, 1992.

(43) Martienssen, W.; Warlimont, H. *Springer Handbook of Condensed Matter and Materials Data*; Springer Science & Business Media, 2006.

(44) Bisio, F.; Palombo, M.; Prato, M.; Cavalleri, O.; Barborini, E.; Vinati, S.; Franchi, M.; Mattera, L.; Canepa, M. Optical Properties of Cluster-Assembled Nanoporous Gold Films. *Phys. Rev. B* **2009**, *80*, 205428.

(45) Bisio, F.; Prato, M.; Cavalleri, O.; Barborini, E.; Mattera, L.; Canepa, M. Interaction of Liquids With Nanoporous Cluster Assembled Au Films. *J. Phys. Chem. C* **2010**, *114*, 17591–17596.

(46) Toccafondi, C.; Uttiya, S.; Cavalleri, O.; Gemme, G.; Barborini, E.; Bisio, F.; Canepa, M. Optical Properties of Nanogranular and Highly Porous TiO2 Thin Films. *J. Phys. D: Appl. Phys.* **2014**, *47*, 485301.

(47) Schulte, C.; Podestà, A.; Lenardi, C.; Tedeschi, G.; Milani, P. Quantitative Control of Protein and Cell Interaction With Nanostructured Surfaces by Cluster Assembling. *Acc. Chem. Res.* **2017**, *50*, 231–239.

(48) Singh, A. V. Biotechnological Applications of Supersonic Cluster Beam-Deposited Nanostructured Thin Films: Bottom-Up Engineering to Optimize Cell–Protein–Surface Interactions. *J. Biomed. Mater. Res. Part A* **2013**, *101*, 2994–3008.

(49) Bisio, F.; Prato, M.; Barborini, E.; Canepa, M. Interaction of Alkanethiols With Nanoporous Cluster-Assembled Au Films. *Langmuir* **2011**, *27*, 8371–8376.

(50) Janczak-Rusch, J.; Chiodi, M.; Cancellieri, C.; Moszner, F.; Hauert, R.; Pigozzi, G.; Jeurgens, L. Structural Evolution of Ag–Cu Nano-Alloys Confined Between AlN Nano-Layers Upon Fast Heating. *Phys. Chem. Chem. Phys.* **2015**, *17*, 28228–28238.

(51) Corbelli, G.; Ghisleri, C.; Marelli, M.; Milani, P.; Ravagnan, L. Highly Deformable Nanostructured Elastomeric Electrodes With Improving Conductivity Upon Cyclical Stretching. *Adv. Mater.* **2011**, *23*, 4504–4508.

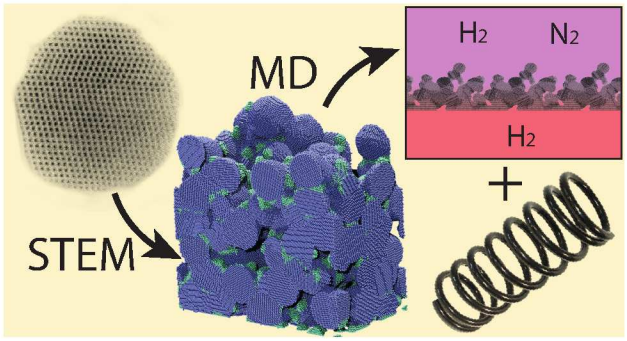
MD
STEM
H2
N2
H2
+